Bioresource Technology Reports 21 (2023) 101301

Contents lists available at ScienceDirect

Bioresource Technology Reports

journal homepage: www.sciencedirect.com/journal/bioresource-technology-reports

Facile synthesis of N, S-modified activated carbon from biomass residue for promising supercapacitor electrode applications

Heri Rustamaji [a,b], Tirto Prakoso [a,*], Hary Devianto [a], Pramujo Widiatmoko [a], Kiki Adi Kurnia [a]

[a] Department of Chemical Engineering, Bandung Institute of Technology, Jl. Ganesha 10, Bandung 40132, Indonesia
[b] Department of Chemical Engineering, Lampung University, Jl. Soemantri Brojonegoro No. 1, Bandar Lampung 35145, Indonesia

ARTICLE INFO

Keywords:
Biomass
N
S modified carbon material
Electrochemical impedance spectroscopy
Electrochemical performance
The electrochemical capacitor

ABSTRACT

This study used hydrothermal carbonization and activation methods to synthesize N, S modified activated carbon (NS-ACA) from biomass residue for supercapacitor electrode application. The process involves calcium chloride as an activating agent and ammonium persulfate as sources of nitrogen and sulfur. The NS-ACA sample's mesoporous structure and specific surface area were 2.9–8.9 nm in diameter and 364.0–677.5 $m^2 \bullet g^{-1}$. The electrochemical analysis revealed that the NS-ACA3 sample is the best result, with a specific capacitance value of 173.91 $F \bullet g^{-1}$ at 0.5 $A \bullet g^{-1}$. The optimum energy and power density values were 5.11 $Wh \bullet kg^{-1}$ and 230.0 $W \bullet kg^{-1}$, respectively, with a current of 0.5 $A \bullet g^{-1}$. The supercapacitor's coulombic efficiency and capacitance retentions were 100 % and 98 %, following 5000 cycles of cyclic charge-discharge testing. The present preparation method is a simple, unique, and promising routine to synthesize dual heteroatoms carbon materials from biomass for high-performance supercapacitors.

1. Introduction

The desire to create sustainable, clean, and green energy storage systems has increased over the last decade (Simon and Gogotsi, 2020). Supercapacitors (SCs) are essential in electrochemical energy storage systems due to their long-life cycle and high power specificity (Gopalakrishnan et al., 2020). This property includes an electrochemical capacitor as an energy storage device with a higher power density than a battery and superior energy-specific than a conventional dielectric capacitor. Furthermore, improved energy storage for supercapacitors has significantly progressed in recent years (Li et al., 2016a, b; Wang et al., 2018). SCs are categorized into two based on how they store energy. They are (1) electric double-layer capacitors (EDLCs), forming capacitance by electrostatic charge separation at the electrode-electrolyte contact, and (2) pseudocapacitors, which store energy based on fast and reversible faradaic redox reactions (Hou et al., 2017; Xie et al., 2016).

There are several investigations of porous carbon materials, such as activated carbon, carbon nanotubes, and graphene as EDLC electrodes (Gao et al., 2015a, b; Liu et al., 2013; Xing et al., 2016). Activated carbon is preferred for commercial supercapacitor devices over other materials because of its wide surface area and inexpensive (Li et al., 2016a, b). However, conventional activated carbons have limited capacitance and power due to their complex and obstructed pore structure, describing the electrolyte ion's pore accessibility at a high charge/discharge rate. Outstanding power output is achieved by minimizing the ion's time to diffuse through electrode materials (Wan et al., 2019). Supercapacitors with pristine carbon materials have poor specific capacitance and energy density, which restricts their application (Thambidurai et al., 2014). Therefore, various initiatives are being made to create excellent-performance supercapacitors with carbon based-electrodes. Chemical stability, high conductivity, a sizable surface area, and controlled pore configuration are requirements for the electrode material for EDLC (Ji et al., 2020).

Insertion of heteroatoms is the most effective strategy to boost the specific capacitance and energy density of carbon material electrodes, including nitrogen, sulfur, phosphor, and boron (Chang et al., 2017; Zhang et al., 2016a, b). Furthermore, heteroatom doping enhances surface wettability, accessibility of electrolyte ions, and electrical conductivity and adds pseudocapacitance (Cai et al., 2017; Li et al., 2013). Pseudocapacitance transfers charges by boosting the carbon electrode's basicity and nitrogen atom's electron donors during nitrogen (N)-insertion. Doping nitrogen into carbon increases the charge/electron carriers, enhancing electrical conductivity (Dujearic-Stephane et al., 2021). The

* Corresponding author.
E-mail address: tirto@che.itb.ac.id (T. Prakoso).

https://doi.org/10.1016/j.biteb.2022.101301
Received 12 October 2022; Received in revised form 25 November 2022; Accepted 29 November 2022
Available online 2 December 2022

porosity of the materials made of carbon was affected by nitrogen, including average pore size, distribution and volume, specific surface area, and acts as an electron donor (Gao et al., 2015a, b).

The synergistic impact of co-doping two heteroatoms rather than a single one improves the overall electrochemical performance (Gopalsamy et al., 2017). Therefore, S atoms protrude from the planar carbon lattice with a bigger size and higher electrochemical activity than the N atoms, generating strain effect and defect sites. The electron spin concentrations on the carbon surface are altered when S atoms (with a greater atomic radius than carbon) are doped, causing varied bond angles and lengths (Kiciński et al., 2014). Consequently, the emphasis on studying heteroatom doping in energy storage materials has increased recently (Zhao et al., 2018).

Porous carbons are produced from various agricultural wastes, including bagasse, coconut and palm shells, maize cobs and stalks, rice husks, and corn stalks, with activating agents like H_3PO_4, KOH, and $ZnCl_2$ (Hu et al., 2014). Empty fruit bunches of oil palm (OPEFB) are agricultural lignocellulose, a plentiful and cost-free renewable waste of palm oil, generated at 48 million tons annually in Indonesia (Statistic Indonesia, 2020). Furthermore, it is typically burned and used as fertilizer, mulching palm oil plants, and mill boiler fuel (Farma et al., 2013). There is various research on the creation of activated carbon from this biowaste for supercapacitors, including Farma et al. (2013), Hendriansyah et al. (2018), Larasati et al. (2019) and Wulandari et al. (2021). However, they have a medium-specific capacitance due to low nitrogen and sulfur content, preventing the highest performance in energy storage devices with highly energetic densities. As a result, mass-producing porous carbons with elevated nitrogen and sulfur concentration from biomass residues through pyrolysis in various experimental situations effectively raises the device's gravimetric capacitance (Zhu et al., 2018).

The KOH and $ZnCl_2$ are the suggested activating agents to enhance the surface area and upgrade the porosity framework despite decreasing the nitrogen concentration of carbon materials (Jain et al., 2015). There are investigations of the chemical activation of waste biomass in producing porous carbon as an adsorbent, replacing KOH and $ZnCl_2$ with calcium chloride ($CaCl_2$) (Lacerda et al., 2015). However, there is a lack of research on synthesizing porous N and S carbon from OPEFB activated by $CaCl_2$. This type of synthesis under appropriate hydrothermal carbonization and activation conditions is less expensive, renewable, straightforward, and environmentally friendly. Therefore, this research aimed to create N, S modified activated carbons with directed and interconnected porosity, utilizing a hydrothermal and activation process of OPEFB raw material employing ammonium persulfate (APS) as nitrogen and sulfur sources. We carefully examined the synergistic impacts of calcium chloride and APS on the permeability structure and activated carbons.

2. Materials and Methods

2.1. Materials

Feedstocks were gathered from the domestic palm oil plant in Indonesia. The chemical reagents used in pure analytical grade include calcium chloride (99.9 wt%, MERCK, CAS-No: 10043-52-4), hydrochloric acid (37 vol%, MERCK, CAS-No. 7647-01-0), and ammonium persulfate (99.9 wt%, Merck, CAS-No: 7727-54-0), polyvinylidene fluoride (99.9 wt%, TOB, CAS No: 24937-79-9). In contrast, ethanol (96 vol%, MERK, CAS-No: 64-17-5) and hydrofluoric acid (55 vol%, Fluka, CAS-No: 7664-39-3) were technical grades supplied by Bratachem Ltd. Whatman filter paper (no. 42) was utilized as a separator in supercapacitor cells produced by GE Healthcare LS. At the same time, the coin cell CR2032 for the case of a supercapacitor was obtained from TMAX Battery equipment, Xiamen, China.

2.2. Synthesis N, S modified activated carbon

The experimental preparation stage was adapted from Wulandari et al. (2021). The raw material in size of 60 mesh diameters was treated with an HF concentration of 1 M for 2 h to take off the ash, filtered, and dried for 24 h in a 105 °C oven. Furthermore, hydrothermal carbonization was conducted by introducing the deashed sample and the $CaCl_2$ solution to the batch reactor, reacting at 275 °C for 1 h. In cold conditions, gas is accommodated in the sampling bag past the sampling valve. The product mixture was accumulated, strained to split the biochar and liquid product, and then dried for an entire night at 110 °C (Jain et al., 2015; Wulandari et al., 2021).

The nitrogen and sulfur (N, S) were altered by mixing APS with hydrochar in 1, 2, and 3 ratios in deionized water, then agitating the mixture at 80 °C for 2 h with a magnetic stirrer, evaporated, and dried. Furthermore, the dried sample was pyrolyzed for activation in a tubular reactor at a temperature of 800 °C. A thermal rate of 10 °C min^{-1} was set by flowing 60 $cm^3 \cdot min^{-1}$ of N_2. Once the temperature of 800 °C was reached, the N_2 gas flow was changed with 60 $cm^3 \cdot min^{-1}$ of CO_2 gas for 2 h to maintain temperature. The reactor was cooled by flowing N_2 gas, and then the carbon product was taken from the reactor, rinsed with 1 M HCl to remove activating agent residue, neutralized, and filtered. Finally, the N, S modified activated carbon was obtained after drying for 2 h at 105 °C (Rustamaji et al., 2022). In addition, AC0 and NS-ACAX denote pure and modified activated carbon, respectively, where X represents the ammonium persulfate to hydrochar proportion.

2.3. Physical characterizations

Scanning electron microscope and energy dispersive spectroscopy (SEM-EDS) were utilized to evaluate the morphology and atomic content of the sample. The carbon sample's X-ray diffraction (XRD) characters were acquired using a Cu target on a Rigaku Ultima IV apparatus (Tokyo, Japan) at 40 kV/20 mA. On a Quantachrome TouchWinTM v1.2 analyzer, the specific surface area was examined using the N_2 adsorption-desorption method. Using Raman spectroscopy (HORIBA Xplora) with a 532 nm blue laser beam, defects resulting from heteroatoms and the degree of graphitization of materials were assessed. A Nicolet 6700 FTIR spectrometer was utilized to characterize the samples' qualitative oxygenated functional groups (OFGs) spanning from 5000 to 450 cm^{-1}. The surface functional group of the samples was evaluated by X-ray photoelectron spectroscopy with Al Kα radiation (XPS, Kratos, Japan).

2.4. Electrochemical characterization

The electrochemical characterization was applied to a full supercapacitor cell. The electrodes were produced by combining activated carbon and 10 % PVdF binder. The material mixture was disseminated in ethanol and incorporated by ultrasonication for 30 min. The prepared material was then slapped and compacted at ~8 MPa to create an electrode with a 15-mm diameter and 1-mm thickness, respectively. A supercapacitor of the coin cell (CR2032) type was constructed using the symmetrical ~2.5 mg cm^{-2} weight of electrodes. Using an electrolyte solution of 6 M KOH, a Whatman filter paper separated the two electrodes, and then the cell was squeezed using a hydraulic press. The cell's electrochemical characteristic was explored by applying a Gamry Reference3000 potentiostat. Cyclic voltammetry (CV), galvanostatic charge-discharge (GCD), and electrochemical impedance spectroscopy (EIS) at 10^{-2}–10^5 Hz. The cycle stability analysis was performed by employing cyclic charge-discharge characterization. The specific capacitance, C_{sp}, was evaluated using Eqs. (1) and (2) to quantitatively related the capacitance value of certain electrode materials (Senthilkumar et al., 2013).

$$C_{cell} = \frac{I\Delta t}{m\Delta V} \quad (1)$$

$$C_{sp} = 4C_{cell} \quad (2)$$

With C_{cell} defined as the cell's gravimetric capacitance ($F \bullet g^{-1}$), m is the entire mass of both electrodes (g), Δt is discharge time (s), ΔV is the potential range after IR-drop (V), and I is applied current (A). Eqs. (3) and (4) were used to evaluate the specific energy, E_{cell} ($Wh \bullet kg^{-1}$), and power, P_{cell} ($W \bullet kg^{-1}$), from the GCD test (Zhou et al., 2016).

$$E_{cell} = \frac{1}{2}\frac{C_{cell}\Delta V^2}{3.6} \quad (3)$$

$$P_{cell} = \frac{E_{cell} \bullet 3600}{\Delta t} \quad (4)$$

3. Results and discussions

3.1. Morphology and structure characterization

The morphological structure of activated carbon was examined by SEM-EDS. Fig. S1a–d in the Supporting Information shows the topology of the linked porous network with crinkles in an SEM image of the AC0 sample and the shape of modified activated carbon with varying APS doping ratios, respectively. The N, S modified activated carbon samples have a porous network structure interconnected with pore clusters (Zhou et al., 2016), while the example's granular morphology has several uneven pores on the surface. Furthermore, morphology and exceptional cavities are critical for energy storage. Previous research found that pores improve ion energy storage. The development of a number of harsh porosities on top of the material surface is linked to the breakdown of lignocellulosic feedstock at high temperatures, evaporating the violent compounds and departing newly formed cavities (Thines et al., 2016).

XRD was utilized to examine the crystallographic structure of activated carbon. Fig. S2 in the Supporting Information depicts the XRD of pure and N, S modified activated carbon samples at various doping ratios. The pieces' XRD curves exhibited a prominent peak and weak band, namely 002 at 2θ by 26° and 100 at 2θ by 43°, respectively. According to JCPDS card no. 41-1487 (Hou et al., 2015), scattering in this layer belonged to hexagonal graphite. Furthermore, the peak at (100) indicated that the carbon material contained a graphitic structure, while the broad peak (002) displayed amorphous structure properties from the activation process. Fig. S2 also shows that the peak intensity (100) of the modified activated carbon is lower than that of ordinary activated carbon, indicating a reduced graphitic structure due to the addition of APS doping (Zhou et al., 2015).

Raman spectra tested the degree of graphitization of activated carbon samples. Fig. S3 in the Supporting Information depicts the Raman spectrum of pure and modified activated carbon as a function of APS proportion. In general, the activated carbon had two substantial peaks at 1590 cm^{-1} for the band of disordered D and 1341 cm^{-1} for graphitic G, implying a perfect and uneven graphite lattice. The D or disruption band, made of sp^3 hybridized carbon at the edge of the graphene, demonstrates the extent of the structural flaw in graphite. The G band represented the sp^2 hybridized carbons from the graphitic plane's C—C bond stretch.

Furthermore, the D and G band proportion explained the number of structural faults connected to sp^3 carbon (Barczak and Bandosz, 2019). The addition of heteroatomic to biomass-based activated improved the defect effect. The number of defects increased the intensity of the D peak and reduced the G peak intensity and graphitization (Zhou et al., 2016). Fig. S3 demonstrates heteroatomic doping gives more defects than undoped activated carbon despite the increased defect porosity. The activated carbon, with a value of 1.21 with doping, exhibited the highest I_D/I_G ratio. Furthermore, its structure changed slightly with increasing doping material, lowering the I_D/I_G proportion value to 1.09 and 1.02, respectively. Raman's research revealed that ratio doping of 3 caused the slightest structural flaws, part of which resulted from the addition of atoms to OPEFB-activated carbon (Dujearic-Stephane et al., 2021).

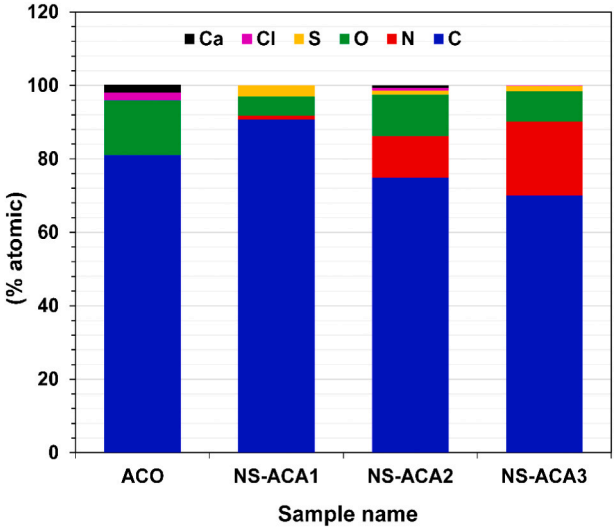

Fig. 1. Element content resulted from SEM-EDS measurement.

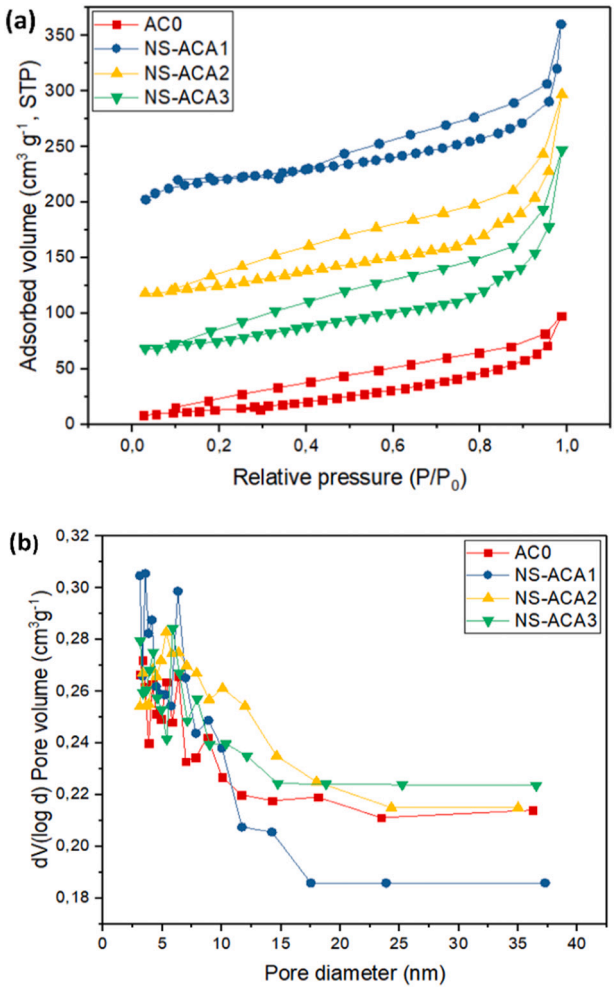

Fig. 2. (a) Nitrogen volume of isotherms adsorption and (b) pore diameter distribution of four sample.

Table 1
Properties of the activated carbon porous structure.

No	Material	S_{BET} ($m^2 \bullet g^{-1}$)	d_p (nm)	V_{total} ($cm \bullet g^{-1}$)
1	AC0	364.00	3.20	0.23
2	NS-ACA1	677.50	3.10	0.31
3	NS-ACA2	558.76	2.91	0.32
4	NS-ACA3	440.24	8.90	0.30

Fig. 1 shows the quantified elements in activated carbon using EDS analysis. The APS to hydrochar ratio favorably affected the quantity of nitrogen and sulfur atoms in activated carbon, indicating that a higher percentage increased nitrogen and reduced sulfur atoms. Each sample had a nitrogen content of 1.15, 10.40, and 20.15 % for NS-ACA1, NS-ACA2, and NS-ACA3. The sulfur content was 3.01, 0.45, and 1.45 %, respectively.

The influence of the APS proportion on the functional groups of the modified activated carbon was investigated using FTIR spectroscopy in the streamer region 5000–450 cm^{-1}, as depicted in Fig. S4 in the Supporting Information. The absorption band at 3450 cm^{-1} was brought on by the stretching vibration of the O—H bond (Zhou et al., 2015). In addition, the bands at 2371 cm^{-1} demonstrated an O═C═O bond, and the peaks at 2935 cm^{-1} and 2860 cm^{-1} exhibited C—H stretching vibration bonding. In contrast, the spectra at 1583 cm^{-1} and 1463 cm^{-1} denoted a C═C bond and a C≡N asymmetric stretching vibration. The C—O bonds, comprising esters and primary alcohols, were represented by the bands around the frequency of 1072–1141.9 cm^{-1}, whereas a spectrum of 951 cm^{-1} showed the ═C—H bond. The wobbling of the C═S bond and the stretching of the S—S bond in the scope were at 732 cm^{-1} and 597 cm^{-1}, respectively (Shabik et al., 2020). The FTIR analysis revealed that nitrogen and sulfur atoms bonded to the modified activated carbon.

The analysis of activated carbon porosity focused on nitrogen adsorption characteristics as open or closed based on the size and accessibility of the pores. Fig. 2a shows N_2 isotherms of adsorption-desorption of each modified activated carbon. Each sample had a type-IV isotherm with a strong hysteresis loop in the 0.20–0.98 P/P_0 range. They show the mesoporous structure formed from hydrothermal carbonization followed by the pyrolysis process (Zhang et al., 2016a, b). At the P/P_0 value of precisely 0.97, N_2 volume increased significantly, indicating substantial voids or mesopores, especially for the APS doping. Fig. 6a shows how the volume adsorbed decreased with an increased doping ratio.

Meanwhile, Fig. 2b exhibits the mesoporous character of activated carbon through the pore size distribution in sizes around 3.3 to 38 nm in diameter. Additionally, it presents the distribution of pore sizes with various tight peaks ranging from 4.2 to 5.5 nm in four samples, confirming the impact of the doping ratio on pore structure. Table 1 shows BET surface area (S_{BET}), average pore diameter (d_p), and total pore volume (V_{total}) of activated carbon samples.

APS doping positively affects the increased surface area of modified activated carbon. However, the increased doping ratio decreased the surface area of altered activated carbon. This decrease was caused by the partial collapse of the pore structure from excess doping compounds (Zhu et al., 2018). Additionally, it was due to a reduction in the effect of defects and an increase in the graphitic structure of activated carbon from increased doping compounds (Treeweranuwat et al., 2020). An increase in the graphitic form was confirmed by the XRD and Raman analysis, showing a slight increase in the degree of graphitization with increased doping compounds. Furthermore, the defect from additional APS was good at a low doping ratio than in ordinary activated carbon.

Various parameters cause the porous structure of N, S-modified activated carbon from waste with a $CaCl_2$ activation (Liu et al., 2016). In the hydrothermal carbonization stage, the activator significantly reduced the amount of water the lignocellulose substances retained. At the same time, their species leaked into the biomass framework. Furthermore, the basic crystal structure was modified, and $CaCl_2$ was added to improve its widespread penetration of biomass. The APS as a nitrogen and sulfur developer was introduced in the hydrochar impregnation stage. At the same time, NH_3 was created by insitu breakdowns of ammonia precursors from APS mixed with the carbon at high temperatures activation, aggregating a widespread $CaCl_2$ to form $CaCl_2 \bullet 2H_2O$ crystals (JCPDS: 70-0385).

As the structure's porosity developed, the activation process produced macro, micro, and mesopores cohabitation. Furthermore, it had nitrogen functional groups inserted into the structure. A porous nitrogen-doped carbon was identified by graphitic degree, an enormous specific surface area, and a distinctive shape. After being washed with deionized water and HCl, the interaction between calcium and soluble carbonates created calcium chloride and a small quantity of calcium carbonate ($CaCO_3$), creating a highly porous nitrogen-rich carbon (Peng et al., 2016). The porous characteristics of synthetic values for various activated carbons reported in the literature were compared, as seen in Table 2.

The properties of the biomass (such as the proximate parameters), the type of activator, the hydrothermal duration, the doping proportion, and the pyrolisis activation temperature significantly impact the characteristics of biomass-based activated carbon. In other words, activated carbons with various properties can be made using different source materials and activation techniques. Varied activating agents used to synthesize activated carbon from the same biomass will result in distinct surface areas. $CaCl_2$-based-activated carbon has a lessen surface area than KOH and $ZnCl_2$ due to variances in its dehydrating and oxidizing actions and molecular dimension. $CaCl_2$ is less expensive instead of $ZnCl_2$, nevertheless. A viable activation procedure should consider cost and activation efficiency (Dang et al., 2020).

The N, S modified activated carbon was confirmed by XPS evaluation. As shown in Fig. S5a in the Supporting Information, five different peaks of the O 1s, N 1s, C 1s, S 2s, and S 2p spectrum are evident at 530, 399, 284, 230, and 168 eV, respectively, demonstrating that N and S

Table 2
Porosity characteristics of activated carbon prepared from distinct raw material.

Carbon source	Activating agent	S_{BET} ($m^2 \bullet g^{-1}$)	V_{total} ($cm^3 \bullet g^{-1}$)	d_P (nm)	Reference
Oil palm empty fruits bunch	KOH	1704	0.89	2.24	(Farma et al., 2013)
Oil palm empty fruits bunch	$ZnCl_2$	1571	–	2.13	(Hendriansyah et al., 2018)
Sugar cane bagasse	$CaCl_2$	805.5	0.68	3.38	(Liu et al., 2016)
Pomelo mesocarps	$CaCl_2$	974.6	0.69	2.9	(Peng et al., 2016)
Cocoa shell	$ZnCl_2$	619	0.32	4.8	(Saucier et al., 2015)
Rice husk	H_3PO_4	298	1.19	2.5	(Somasundaram et al., 2013)
Rice husk	H_3PO_4	1493	1.21	3.25	(Ganesan et al., 2014)
Sago waste	$ZnCl_2$	546.6	0.30	3.3	(Togibasa et al., 2021)
Firewood	K_2CO_3	818	0.44	2.1	(Lu et al., 2016)
Durian shell	KOH	180	0.093	1.1	(Kanjana et al., 2021)
Rubber seed shell	KOH	148	0.067	1.2	(Kanjana et al., 2021)
Palm petiole	KOH	436	0.241	1.2	(Kanjana et al., 2021)
N, S-modified empty-fruits bunch	$CaCl_2$	677.5	0.31	3.1	This work

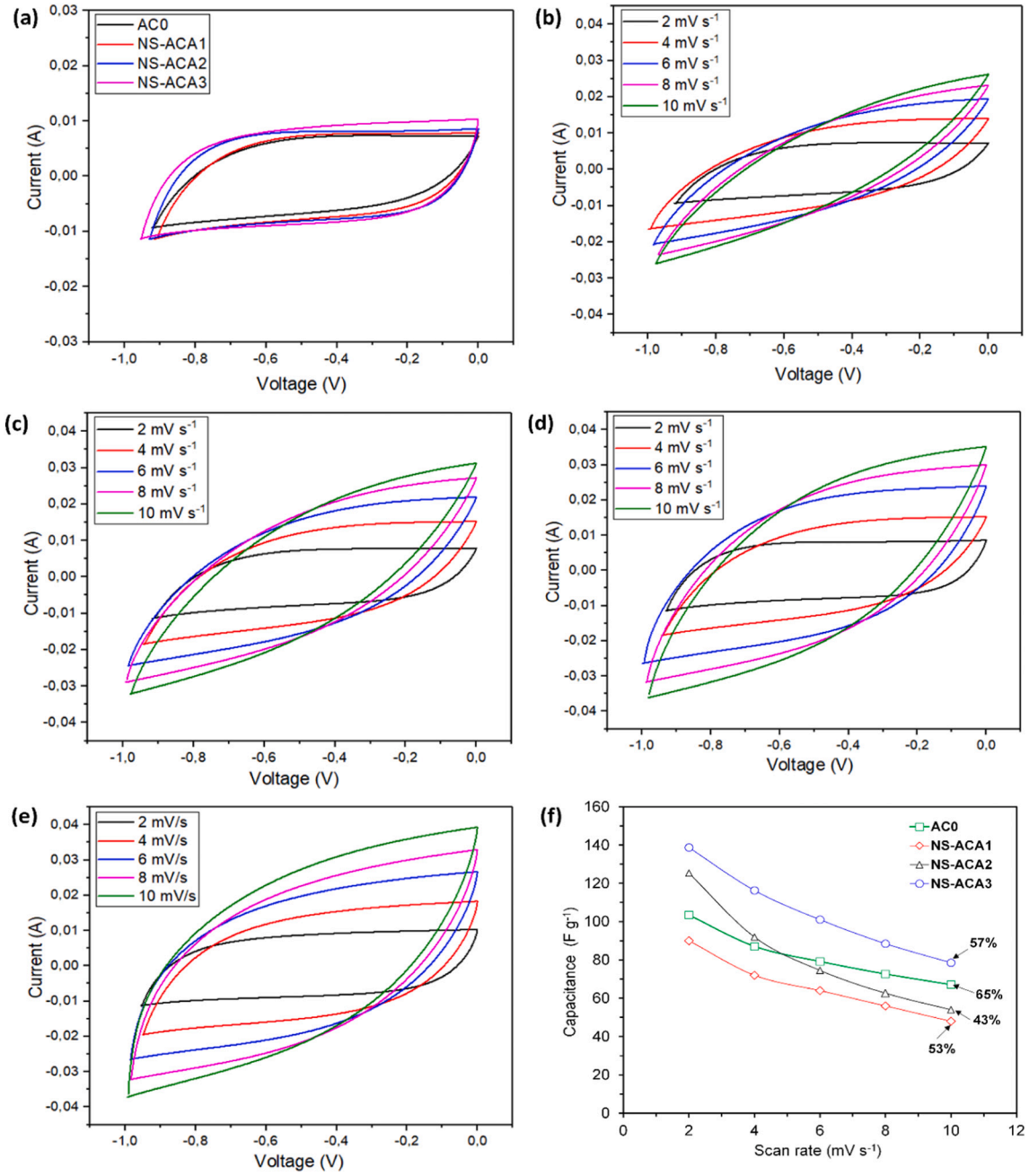

Fig. 3. Cyclic voltammograms of fabricated cells. (a) All of the material at 2 mV•s^{-1}, (b) AC0, (c) NS-ACA1, (d) NS-ACA2, (e) NS-ACA3 at various scan rates, and (f) the rate capability curve.

were inserted into the structure of NS-ACA3 (Zhou et al., 2016). On the other hand, in the AC0 sample, the atomic signals of N 1s, S 2s, and S2p do not appear. It is already that the process of modifying N and S is successful.

Three properties of the C structure are shown by the high-resolution C 1s XPS spectrum (Fig. S5b), such as aromatic conjugated sp^2 C (C═C) at 284.4 eV, the sp3 C (C—N, C—O, and C—S) at 285.6 eV, and the C═O/C═N at 288.1 eV (Liu et al., 2017). According to the high-resolution N 1s spectrum (Fig. S5c), the modified N atoms were in the pyridinic-N (398.5 eV), pyrrolic (400.5 eV), quaternary-N (401.5 eV), and pyridine-N-oxides bonding arrangements (402.6 eV) (Zhang et al., 2020). Due to their outstanding electron-donor properties, pyridinic and pyrrolic have excellent charge mobility, which may also increase the electrochemical reactivity of carbon material surfaces (Liu et al., 2016). Quarternary is highly helpful in increasing the conductivity of carbon materials due to the partial substitution of N atoms for carbon atoms in graphite crystallites (Peng et al., 2016; Saucier et al., 2015). As a surface functional group, pyridine-N-oxides will also significantly impact the carbon material's wettability (Ji et al., 2020).

NS-ACA3 reveals a clear S atom spectrum, as shown in Fig. S5d. Two peaks can match the S 2p orbit with binding energies of 168.1 and 169.4, which are assigned to the various oxidation states of C—SOx—C obtained from the plane of the carbon falseworks. In contrast to the N element, the S element will enhance the polarization and electron density of the carbon surface when inserted into a carbon matrix, and its oxygen-comprising functional groups (such as sulfoxide and sulfone) will add ancillary pseudocapacitance (Zhou et al., 2016). Therefore, the high amount of sulfoxide and sulfone is favorable for the specific capacitance of N, S-doped carbon.

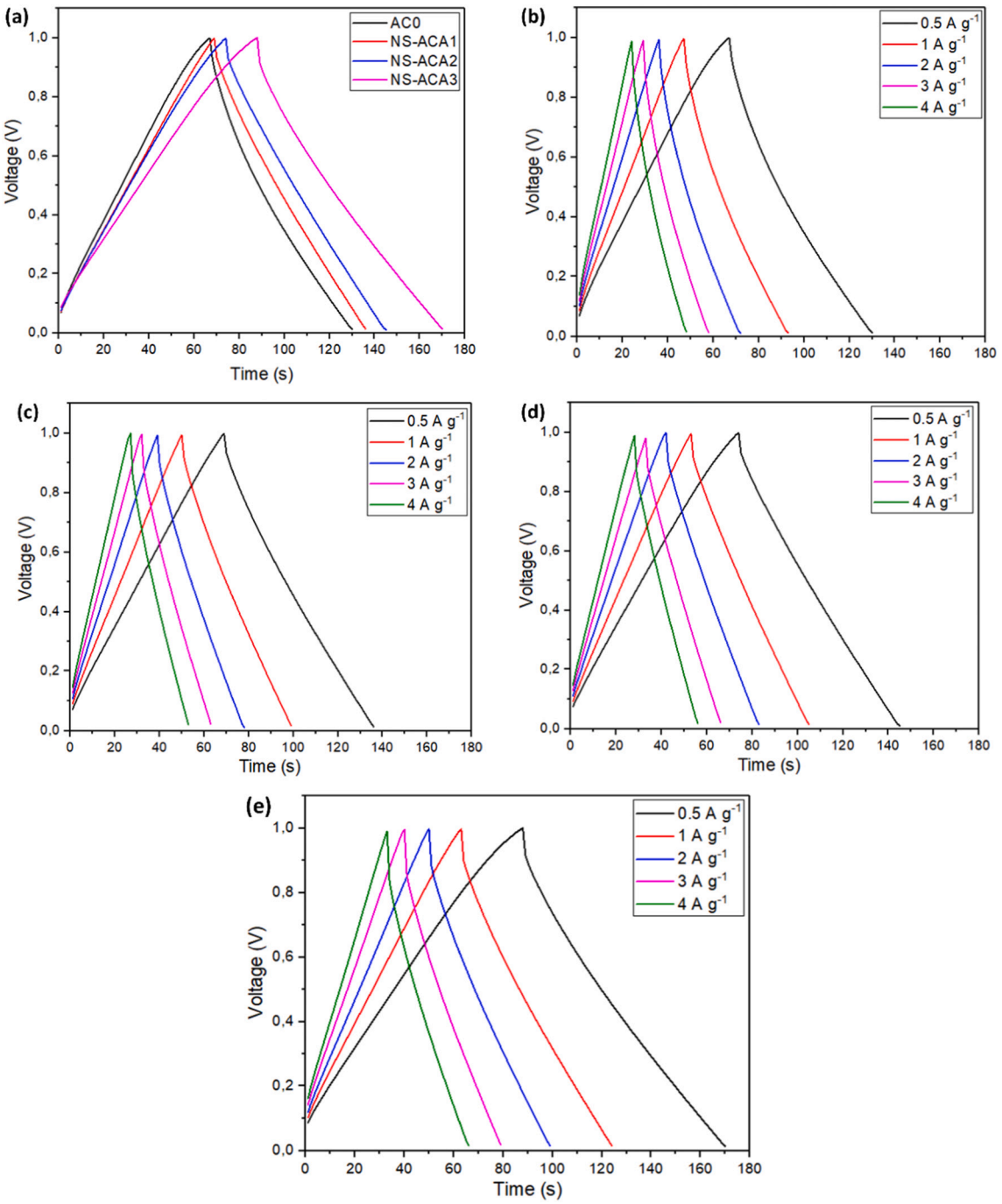

Fig. 4. Charging and discharging curves resulted from galvanostatic assessment. (a) All of the material at 0.5 A•g^{-1}, (b) AC0, (b) NS-ACA1, (c) NS-ACA2, and (d) NS-ACA3.

3.2. Electrochemical characterization

The electrochemical characteristics of all materials were performed on full supercapacitor cells. The CV curve determined the cell's properties and the supercapacitor's specific capacitance value. Fig. 3a illustrates the CV analysis for modified (NS-ACA) and pure activated carbon (AC0) supercapacitors with a scan rate of 2 mV•s^{-1}.

Each material's cyclic voltammogram had a perfect quasi-rectangle shape with no redox peaks. Main electricity and double-layer capacitance were generated due to numerous adsorbed ions on the electrode's surface with the electrolyte's diffusion threshold, shown by the cyclic voltammogram's excellent rectangular shape. Furthermore, the voltammogram curve was an oblique parallelogram with an increased scan rate, indicating rapid charging-discharging with minimal series resistance and robust power deliverability (Cao et al., 2018). The NS-ACA3 curve presented the sample's biggest covered region, denoting the maximum capacitance. Fig. 3b–e exhibits the voltammogram at 2–10 mV•s^{-1} for AC0, NS-ACA1, NS-ACA2, and NS-ACA3, respectively.

The greater scan rate caused more parallelograms of the cyclic voltammogram plots for all supercapacitors. Lacking redox plateaus confirms the lack of pseudocapacitive occurrence and excellent performance (Wan et al., 2019). Fig. 3f shows the specific capacitance values from Eq. (2) at different scan rates, which grow with the increased number of dopants. However, adding N and S at the doping ratio of one increases the capacitance insignificantly due to low doping. The results demonstrated that a faster scan rate lowered the particular

Table 3
Activated carbon-based supercapacitor performance at 0.5 A g^{-1}.

No.	Material	C_{sp} (F•g^{-1})	E_{cell} (Wh•kg^{-1})	P_{cell} (W•kg^{-1})
1	AC0	130.43	3.83	145.30
2	NS-ACA1	141.30	4.15	166.10
3	NS-ACA2	163.30	4.79	215.60
4	NS-ACA3	173.91	5.11	230.00

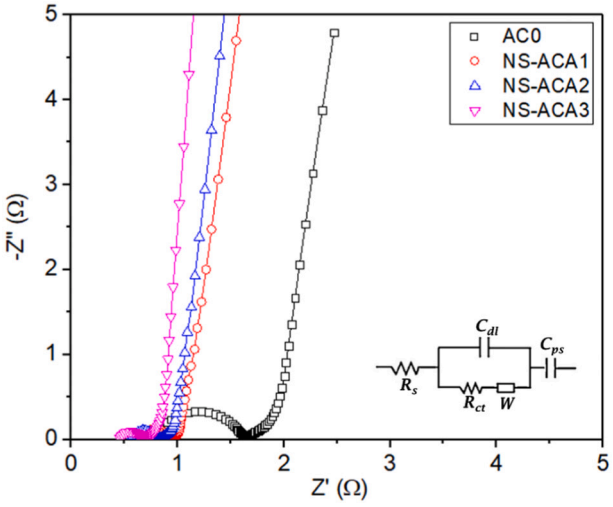

Fig. 5. The EIS-Nyquist curve of four samples.

capacitance value. The cyclic voltammogram in low scan rates showed perfect capacitive behavior. Increased scan rate increased disturbed the ideal behavior, continuously dropping the capacitance. This phenomenon is common in activated carbon materials because of not enough time for ion transfer and adsorption inside the irregular pore structure of particles. Reduced capacitance indicates that not all pore structures are accessible at higher scan rates due to the resistance in the movement of ions from the electrolyte to the internal area of the pores (Si et al., 2013).

Fig. 3f shows that AC0-based supercapacitor cells have the highest rate capability at 65 %. Furthermore, samples with N and S doping had a lower capability level of 53, 43, and 57 % for NS-ACA1, NS-ACA2, and NS-ACA3, respectively. Rate capability was affected by the massive mesoporous structure, and the high specific surface area permits more active sites for ion adsorption. Enriching the electrode material with nitrogen and sulfur improved wettability and hydrophilicity and promoted ion movement (Liang et al., 2019). In conclusion, the N and S doping boosted the supercapacitor-specific capacitance of biomass-based-activated carbon but lowered the rate capability. Oversized doping degraded the material's structure by disordering the pore system, reducing the electron transport efficiency (Zhou et al., 2016).

The characteristics of the supercapacitor voltage response to time measured at a certain current are shown by a charge/discharge graph in Fig. 4. Charge-discharge measurements indicate the rate of the charging-discharging process and the range of cell voltages achieved (Yu et al., 2021), performed at a specific current of 0.5–4 A•g^{-1}. All the sample scarves in Fig. 4 had a symmetrical triangular formation. This kind of graph is typical in supercapacitor devices made of activated carbon (Farma et al., 2013). The voltage reduction denoted an imperfect charge/discharge process, indicating a partial ions' desorption at a specific current.

Furthermore, a reaction between the electrolyte and electrode ions produced an equivalent series resistance. According to this research, the supercapacitor cell has a superior power character because of its minimal voltage drop (Li et al., 2016a, b). The charge/discharge plot was employed to ascertain the secure operating voltage for supercapacitor

Table 4
Capacitance and resistance value of activated carbon based-supercapacitor from the equivalent circuit.

No.	Material	C_{dl} (F)	C_{ps} (mF)	R_s (Ω)	R_{ct} (Ω)
1	AC0	6.72	0.67	0.78	0.82
2	NS-ACA1	6.85	2.06	0.60	0.33
3	NS-ACA2	8.13	4.07	0.55	0.28
4	NS-ACA3	9.05	7.25	0.46	0.23

cells, shown as 0.8–1.0 V in Fig. 4 (Dujearic-Stephane et al., 2021).

Table 3 shows the results for Eqs. (3) and (4) calculating the energy and power densities, with the highest and lowest specific energy of 5.11 Wh•kg^{-1} and 3.83 Wh•kg^{-1} in NS-ACA3 and AC0, respectively. Furthermore, the maximum specific density was 230 W•kg^{-1} for the NS-ACA3 sample, while the lowest was 145.30 W•kg^{-1} for AC0. The redox effect and conductivity improvement of the modified activated carbon demonstrated that the N and S doping increased the energy and power density (Dang et al., 2020).

The supercapacitor's electrochemical parameters, the electrolyte/electrode interface resistance, and ion transfer in porous resistance were characterized using EIS in a frequency range from 10^{-2} to 10^{5} Hz, displaying the curve in a Nyquist plot. Fig. 5 shows the Nyquist plot of the four samples and the equivalent circuit for fitting the EIS data achieved by the Echem Analyst software (the inset). A perfect supercapacitor cell in high, medium and low frequencies has a semicircular, slash (45°), and perpendicular (90°) Nyquist curve, respectively. Furthermore, the electrolyte's resistance (R_s) is represented at the beginning of the semicircle. From the Nyquist plot, it can be obtained that the electrolyte resistance, R_s for AC0, NS-ACA1, NS-ACA2, and NS-ACA3 was 0.79, 0.61, 0.56, and 0.45 Ω for each sample, respectively. The samples in medium-high frequencies revealed full and partial semicircular loops with their form, indicating the cell's impedance impacted by charge transfer resistance (R_{ct}) at the interface between the electrolyte and electrode. Their R_{ct} values in the semicircle shape were 0.81, 0.34, 0.27, and 0.24 Ω. The slanted segment of the curve (about 45) in the intermediate frequencies is attributed to the Warburg impedance (W), which was resistance in ion transport into the electrode pores at medium to low frequencies (R_w) (Mei et al., 2018). The R_w value were 0.30, 0.15, 0.14, and 0.12 Ω, respectively. At low frequencies, the imaginary part of the impedance increases, corresponding to the ideal capacitive behavior of carbons.

The N and S concentrations in a smaller semicircle lowered the charge transfer resistance at the electrolyte/electrode interface (Wang et al., 2015). Furthermore, nitrogen and sulfur in the electrode affected the electrolyte's wettability and improved conductivity. The

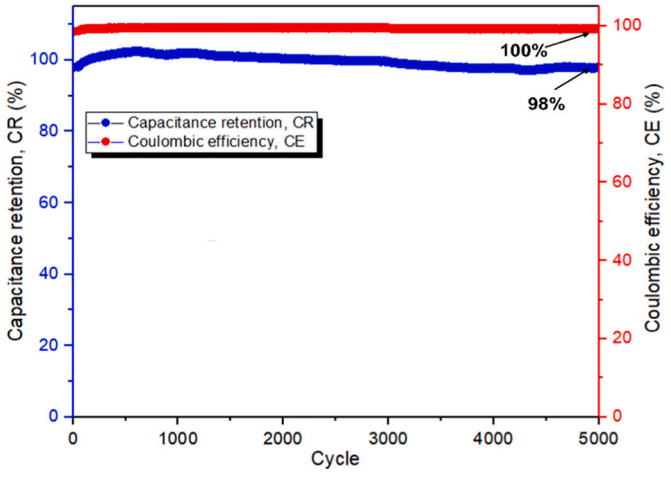

Fig. 6. Cyclic stability of NS-ACA3 samples at 5000 cycles.

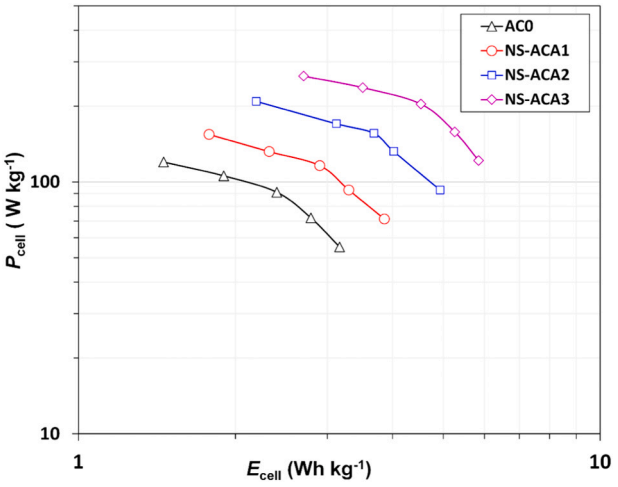

Fig. 7. Ragon plot of four samples.

supercapacitor's rate capability is expanded by an electrolyte and a low charge transfer resistance (Cao et al., 2018). The EIS curve demonstrated that nitrogen and sulfur doping of activated carbon reduced the resistance of electrolyte and charge transfer. Ion transfer resistance in the porous decreased with an increased doping ratio, although the pore diameters were relatively similar. Additionally, lower mass transfer resistance was due to increased wettability (Zhang et al., 2016a, b).

Table 4 shows the fitting parameter values based on the equivalent circuit of the Nyquist plot, which follows other research (Si et al., 2013). The measured capacitance is the actual capacitance of the electrode mass load. C_{dl} is a double-layer capacitor, and C_{ps} is a boundary pseudocapacitor produced by a redox reaction of a heteroatom-containing group, the value of which increases with an increase in the amount of N and S doping.

A cyclic charge-discharge (CCD) assessment was used to verify the supercapacitor's cyclic stability and endurance, as depicted in Fig. 6. A specific voltage and current were used to obtain the supercapacitor's charge and discharge during a predetermined cycle. Additionally, the coulombic efficiency (CE) and capacitance retention (CR) values were used to compute the device's life cycle. The CE represents the discharge-to-charge capacity ratio for the current process (Zhou et al., 2016), while CR is the capacitance ratio of every cycle to its beginning. The CE values for NS-ACA3-based supercapacitors remained constant for 5000 cycles, with 100 %; hence the CR values were stable at 98 %. The electrochemical assessment results revealed that modified activated carbon with N and S doping effectively increased the specific capacitance and maintained coulomb efficiency but decreased the capacitance retention. High CE indicates a low risk of adverse reactions at the electrode surface (Rustamaji et al., 2022).

The energy density and power density of the symmetric supercapacitor on the Ragone plot are displayed in Fig. 7, demonstrating that the AC0 sample has the lowest energy density. In contrast, adding N and S doping to the sample increases the energy density for the NS-ACA1, NS-ACA2, and NS-ACA3 samples, respectively. The carbon material's surface polarity is substantially enhanced by heteroatom functionalities, improving the specific electrostatic interactions between the electrode's active surface and the electrolyte ions. The obvious benefit is that the modified space-charge-layer capacitance increases specific capacitance by improving electrode wettability because there are more hydrophilic polar sites and declining equivalent series resistance. The functional groups formed on the carbon surface go through faradic redox reactions, which contribute to pseudocapacitance and thus improve overall capacitance. This event ultimately enhances the supercapacitor's energy density (Hasegawa et al., 2015). These results indicate that N, S modified activated carbon could boost energy density.

Table 5 compares the characteristics of various supercapacitors employing electrodes of biomass-based-activated carbon. The cycle stability of the supercapacitor results from this study shows a higher value at a longer cycle than the reference (Farma et al., 2013; Mei et al., 2018). The capacitance value of this experiment is quite competitive compared to the previously published electrode materials in Table 5, which suggests that N, S modification of biomass is a viable technique for improving the capabilities of supercapacitors.

4. Conclusions

The hydrothermal and activation methods effectively synthesized a novel N, S-modified activated carbon (NS-ACA) with APS. The NS-ACA's mesoporous structure had a specified surface area of 440.24–677.50 $m^2 \bullet g^{-1}$. Furthermore, increasing APS to hydrochar increased and decreased the nitrogen and sulfur atom content, respectively. The highest capacitance value at 173.91 $F \bullet g^{-1}$ at 0.5 $A \bullet g^{-1}$ in 6 M KOH electrolyte for the NS-ACA3 sample. The assembled symmetric supercapacitor had an operating potential of 0.8–1.0 V and maximum energy, power, and energy density of 5.11 $Wh \bullet kg^{-1}$, 230.0 $W \bullet kg^{-1}$, and 0.5 $A \bullet g^{-1}$, respectively. Coulombic efficiency was maintained at 100 %, while the retention capacitance was 98 % in the 5000-cycle test. Modifying N and S increased activated carbon's specific capacitance and lowered the rate capability and cycle stability. Furthermore, these outcomes implied that palm oil waste could be recycled and utilized for activated carbon products.

CRediT authorship contribution statement

Conceptualization, TP and HD; Methodology, HR and HD; Formal analysis, HR, TP, HD; Investigation, HR; Resources, TP and PW; Data curation, HR, TP, HD, KAK; Writing – original draft preparation, HR; Writing – review and editing, TP, PW, and KAK; Visualization, TP and KAK; Supervision, TP and HD; Project administration, PW; Funding acquisition, TP All authors have read and agreed to the published version of the manuscript.

Declaration of competing interest

The authors declare that they have no known competing financial interests or personal relationships that could have appeared to influence

Table 5
Electrochemical characteristics of diverse biomass or biowaste-derived activated carbon electrodes.

Biomass	Electrolyte	C_{sp} ($F \bullet g^{-1}$)	E_{cell} ($Wh \bullet kg^{-1}$)/P_{cell} ($W \bullet kg^{-1}$)	Stability (%)/cycle	References
Oil palm empty fruits bunch	1 M H_2SO_4	150 (10 $mA \bullet cm^{-2}$)	4.3/173.3	–	(Farma et al., 2013)
Rice husk	1 M Na_2SO_4	112 (1 $A \bullet g^{-1}$)	15.5/1421	–	(Ganesan et al., 2014)
Durian shell	1 M KOH	178 (1 $A \bullet g^{-1}$)	–	99/4000	(Kanjana et al., 2021)
Rubber seed shell	1 M KOH	123 (1 $mA \bullet cm^{-2}$)	–	–	(Kanjana et al., 2021)
Modified-coconut shell	6 M KOH	179 (0.5 A g^{-1})	–	84/2500	(Yang et al., 2018)
Rotten carrot	1 M $LiClO_4$	142.7 (1 mA cm^{-2})	28.4/89,100		(Ahmed et al., 2018)
Pulp sludge	1 M $TEABF_4$	120 (10 $A \bullet g^{-1}$)	14.7/90		(Wang et al., 2013)
Hemp fibers	1 M H_2SO_4	122 (10 $A \bullet g^{-1}$)	–	–	(Mijailović et al., 2017)
N, S-modified-oil palm empty fruits bunch	6 M KOH	173.91 (0.5 $A \bullet g^{-1}$)	5.11/230.0	98/5000	This work

the work reported in this paper.

Data availability

Data will be made available on request.

Acknowledgment

This research was grateful to the Indonesia Endowment Fund for Education (Lembaga Pengelola Dana Pendidikan, LPDP) for providing the BUDI-DN scholarship (No. 2020022102189).

Appendix A. Supplementary data

Supplementary data to this article can be found online at https://doi.org/10.1016/j.biteb.2022.101301.

References

Ahmed, S., Ahmed, A., Rafat, M., 2018. Supercapacitor performance of activated carbon derived from rotten carrot in aqueous, organic, and ionic liquid-based electrolytes. J. Saudi Chem. Soc. 22, 993–1002. https://doi.org/10.1016/j.jscs.2018.03.002.

Barczak, M., Bandosz, T.J., 2019. Evaluation of nitrogen and sulfur-doped porous carbon textiles as electrode materials for flexible supercapacitors. Electrochim. Acta 305, 125–136. https://doi.org/10.1016/j.electacta.2019.03.014.

Cai, Y., Luo, Y., Dong, H., Zhao, X., Xiao, Y., Liang, Y., Hu, H., 2017. Hierarchically porous carbon nanosheets derived from Moringa oleifera stems as electrode material for high-performance electric double-layer capacitors. J. Power Sources 353, 260–269. https://doi.org/10.1016/j.jpowsour.2017.04.021.

Cao, H., Peng, X., Zhao, M., Liu, P., Xu, B., Guo, J., 2018. Oxygen functional groups improve the energy storage performances of graphene electrochemical supercapacitors. RSC Adv. 8, 2858–2865. https://doi.org/10.1039/c7ra12425b.

Chang, Y., Zhang, G., Han, B., Li, H., Hu, C., Pang, Y., Chang, Z., Sun, X., 2017. Polymer dehalogenation-enabled fast fabrication of N, S-codoped carbon materials for superior supercapacitor and deionization applications. ACS Appl. Mater. Interfaces 9, 29753–29759. https://doi.org/10.1021/acsami.7b08181.

Dang, F., Zhao, W., Yang, P., Wu, H., Liu, Y., 2020. Nitrogen and sulfur co-doped hierarchical graphene hydrogel for high-performance electrode materials. J. Appl. Electrochem. 50, 463–473. https://doi.org/10.1007/s10800-020-01404-5.

Dujearic-Stephane, K., Gupta, M., Kumar, A., Sharma, V., Pandit, S., Bocchetta, P., Kumar, Y., 2021. The effect of modifications of activated carbon materials on the capacitive performance: surface, microstructure, and wettability. J. Compos. Sci. 5, 66. https://doi.org/10.3390/jcs5030066.

Farma, R., Deraman, M., Awitdrus, A., Talib, I.A., Taer, E., Basri, N.H., 2013. Preparation of highly porous binderless activated carbon electrodes from fibers of oil palm empty fruit bunches for application in supercapacitors. Bioresour. Technol. 132, 254–261. https://doi.org/10.1016/j.biortech.2013.01.044.

Ganesan, A., Mukherjee, R., Raj, J., Shaijumon, M.M., 2014. Nanoporous rice husk-derived carbon for gas storage and high-performance electrochemical energy storage. J. Porous. Mater. 21, 839–847. https://doi.org/10.1007/s10934-014-9833-4.

Gao, F., Shao, G., Qu, J., Lv, S., Li, Y., Wu, M., 2015. Tailoring of porous and nitrogen-rich carbons derived from hydrochar for high-performance supercapacitor electrodes. Electrochim. Acta 155, 201–208. https://doi.org/10.1016/j.electacta.2014.12.069.

Gao, P.C., Tsai, W.Y., Daffos, B., Taberna, P.L., Pérez, C.R., Gogotsi, Y., Simon, P., Favier, F., 2015. Graphene-like carbide-derived carbon for high-power supercapacitors. Nano Energy 12, 197–206. https://doi.org/10.1016/j.nanoen.2014.12.017.

Gopalakrishnan, A., Raju, T.D., Badhulika, S., 2020. Green synthesis of nitrogen, sulfur-co-doped worm-like hierarchical porous carbon derived from ginger for outstanding supercapacitor performance. Carbon 168, 209–219. https://doi.org/10.1016/j.carbon.2020.07.017.

Gopalsamy, K., Balamurugan, J., Duy, T., Hoon, N., Hee, J., 2017. Fabrication of nitrogen and sulfur co-doped graphene nanoribbons with porous architecture for high-performance supercapacitors. Chem. Eng. J. 312, 180–190. https://doi.org/10.1016/j.cej.2016.11.130.

Hasegawa, G., Deguchi, T., Kanamori, K., Kobayashi, Y., Kageyama, H., Abe, T., Nakanishi, K., 2015. High-level doping of nitrogen, phosphorus, and sulfur into activated carbon monoliths and their electrochemical capacitances. Chem. Mater. 27, 4703–4712. https://doi.org/10.1021/acs.chemmater.5b01349.

Hendriansyah, R., Prakoso, T., Widiatmoko, P., Nurdin, I., Devianto, H., 2018. Manufacturing carbon material by carbonization of cellulosic palm oil waste for supercapacitor material. MATEC Web Conf. 156 https://doi.org/10.1051/matecconf/201815603018.

Hou, J., Cao, C., Idrees, F., Ma, X., 2015. Hierarchical porous nitrogen-doped carbon nanosheets derived from silk for ultrahigh-capacity battery anodes and supercapacitors. ACS Nano 9, 2556–2564. https://doi.org/10.1021/nn506394r.

Hou, J., Jiang, K., Tahir, M., Wu, X., Idrees, F., Shen, M., Cao, C., 2017. Tunable porous structure of carbon nanosheets derived from puffed rice for high energy density supercapacitors. J. Power Sources 371, 148–155. https://doi.org/10.1016/j.jpowsour.2017.10.045.

Hu, Y., Liu, H., Ke, Q., Wang, J., 2014. Effects of nitrogen doping on supercapacitor performance of a mesoporous carbon electrode produced by a hydrothermal soft-templating process. J. Mater. Chem. A 2, 11753–11758. https://doi.org/10.1039/c4ta01269k.

Jain, A., Xu, C., Jayaraman, S., Balasubramanian, R., 2015. Mesoporous activated carbons with enhanced porosity by optimal hydrothermal pre-treatment of biomass for supercapacitor applications. Micropor. Mesopor. Mat. 218, 55–61. https://doi.org/10.1016/j.micromeso.2015.06.041.

Ji, L., Wang, B., Yu, Y., Wang, N., Zhao, J., 2020. N, S co-doped biomass-derived carbon with sheet-like microstructures for supercapacitors. Electrochim. Acta 331, 135348. https://doi.org/10.1016/j.electacta.2019.135348.

Kanjana, K., Harding, P., Kwamman, T., Kingkam, W., 2021. Biomass and Bioenergy Biomass-derived activated carbons with extremely narrow pore size distribution via eco-friendly synthesis for supercapacitor application. Biomass Bioenergy 153, 106206. https://doi.org/10.1016/j.biombioe.2021.106206.

Kiciński, W., Szala, M., Bystrzejewski, M., 2014. Sulfur-doped porous carbons: Synthesis and applications. Carbon 68, 1–32. https://doi.org/10.1016/j.carbon.2013.11.004.

Lacerda, V., López-Sotelo, J.B., Correa-Guimarães, A., Hernández-Navarro, S., Sánchez-Báscones, M., Navas-Gracia, L.M., Martín-Ramos, P., Martín-Gil, J., 2015. Rhodamine B removal with activated carbons obtained from lignocellulosic waste. J. Environ. Manag. 155, 67–76. https://doi.org/10.1016/j.jenvman.2015.03.007.

Larasati, T.D., Prakoso, T., Rizkiana, J., Devianto, H., Widiatmoko, P., Nurdin, I., 2019. Nano carbon produced by advanced mild hydrothermal process of oil palm biomass for supercapacitor material. IOP Conf. Ser.: Mater. Sci. Eng. 543, 012031 https://doi.org/10.1088/1757-899X/543/1/012031.

Li, B., Dai, F., Xiao, Q., Yang, L., Shen, J., Zhang, C., Cai, M., 2016. Nitrogen-doped activated carbon for a high-energy hybrid supercapacitor. Energy Environ. Sci. 9, 102–106. https://doi.org/10.1039/c5ee03149d.

Li, Yiju, Wang, G., Wei, T., Fan, Z., Yan, P., 2016. Nitrogen and sulfur co-doped porous carbon nanosheets derived from willow catkin for supercapacitors. Nano Energy 19, 165–175. https://doi.org/10.1016/j.nanoen.2015.10.038.

Li, Yunyong, Li, Z., Shen, P.K., 2013. Simultaneous formation of ultrahigh surface area and three-dimensional hierarchical porous graphene-like networks for fast and highly stable supercapacitors. Adv. Mater. 25, 2474–2480. https://doi.org/10.1002/adma.201205332.

Liang, K., Wang, W., Yu, Y., Liu, L., Lv, H., Zhang, Y., Chen, A., 2019. Synthesis of nitrogen-doped mesoporous carbon for high-performance supercapacitors. New J. Chem. 43, 2776–2782. https://doi.org/10.1039/C8NJ05938A.

Liu, J., Deng, Y., Li, X., Wang, L., 2016. Promising nitrogen-rich porous carbons derived from one-step calcium chloride activation of biomass-based waste for high-performance supercapacitors. ACS Sustain. Chem. Eng. 4, 177–187. https://doi.org/10.1021/acssuschemeng.5b00926.

Liu, N., Shen, J., Liu, D., 2013. Activated high specific surface area carbon aerogels for EDLCs. Micropor. Mesopor. Mater. 167, 176–181. https://doi.org/10.1016/j.micromeso.2012.09.009.

Liu, T., Cui, Z.W., Zhou, J., Wang, Y., Zou, Z.G., 2017. Synthesis of pyridinic-rich N, S co-doped carbon quantum dots as effective enzyme mimics. Nanoscale Res. Lett. 12, 375. https://doi.org/10.1186/s11671-017-2149-y.

Lu, B., Hu, L., Yin, H., Xiao, W., Wang, D., 2016. One-step molten salt carbonization (MSC) of firewood biomass for capacitive carbon. RSC Adv. 6, 106485–106490. https://doi.org/10.1039/C6RA22191B.

Mei, B.A., Munteshari, O., Lau, J., Dunn, B., Pilon, L., 2018. Physical interpretations of Nyquist plots for EDLC electrodes and devices. J. Phys. Chem. C 122, 194–206. https://doi.org/10.1021/acs.jpcc.7b10582.

Mijailović, D.M., Vukčević, M.M., Stević, Z.M., Kalijadis, A.M., Stojanović, D.B., Panić, V. V., Uskoković, P.S., 2017. Supercapacitive performances of activated highly microporous natural carbon macro fibers. J. Electrochem. Soc. 164, A1061–A1068. https://doi.org/10.1149/2.0581706jes.

Peng, H., Ma, G., Sun, K., Zhang, Z., Yang, Q., Lei, Z., 2016. Nitrogen-doped interconnected carbon nanosheets from pomelo mesocarps for high-performance supercapacitors. Electrochim. Acta 190, 862–871. https://doi.org/10.1016/j.electacta.2015.12.195.

Rustamaji, H., Prakoso, T., Devianto, H., Widiatmoko, P., Saputera, W.H., 2022. Urea nitrogenated mesoporous activated carbon derived from oil palm empty fruit bunch for high-performance supercapacitor. J. Energy Storage. 52, 104724 https://doi.org/10.1016/j.est.2022.104724.

Saucier, C., Adebayo, M.A., Lima, E.C., Cataluña, R., Thue, P.S., Prola, L.D.T., Puchana-Rosero, M.J., Machado, F.M., Pavan, F.A., Dotto, G.L., 2015. Microwave-assisted activated carbon from a cocoa shell as adsorbent for removal of sodium diclofenac and nimesulide from aqueous effluents. J. Hazard. Mater. 289, 18–27. https://doi.org/10.1016/j.jhazmat.2015.02.026.

Senthilkumar, S.T., Selvan, R.K., Ponpandian, N., Melo, J.S., Lee, Y.S., 2013. Improved performance of electric double-layer capacitor using redox additive (VO2-/VO2+) aqueous electrolyte. J. Mater. Chem. A. 3, 7913–7919. https://doi.org/10.1039/c3ta10998d.

Shabik, M.F., Begum, H., Rahman, M.M., Marwani, H.M., Hasnat, M.A., 2020. Heterogeneous kinetics of thiourea electro-catalytic oxidation reactions on palladium surface in an aqueous medium. Chem. Asian J. 15, 4327–4338. https://doi.org/10.1002/asia.202001016.

Si, W., Zhou, J., Zhang, S., Li, S., Xing, W., Zhuo, S., 2013. Tunable N-doped or dual N, S-doped activated hydrothermal carbons derived from human hair and glucose for supercapacitor applications. Electrochim. Acta 107, 397–405. https://doi.org/10.1016/j.electacta.2013.06.065.

Simon, P., Gogotsi, Y., 2020. Perspectives for electrochemical capacitors and related devices. Nat. Mater. 19 (11), 1151–1163. https://doi.org/10.1038/s41563-020-0747-z.

Somasundaram, S., Sekar, K., Kumar, V., Ganesan, S., 2013. Synthesis and characterization of mesoporous activated carbon from rice husk for adsorption of glycine from alcohol-aqueous mixture. J. Mol. Liq. 177, 416–425. https://doi.org/10.1016/j.molliq.2012.09.022.

Statistic Indonesia, 2020. In: Indonesian Oil Palm Statistics 2020, 21, pp. 1–9. http://mpoc.org.my/malaysian-palm-oil-industry/.

Thambidurai, A., Lourdusamy, J.K., John, J.V., Ganesan, S., 2014. Preparation and electrochemical behaviour of biomass based porous carbons as electrodes for supercapacitors - a comparative investigation. Korean J. Chem. Eng. 31, 268–275. https://doi.org/10.1007/s11814-013-0228-z.

Thines, K.R., Abdullah, E.C., Ruthiraan, M., Mubarak, N.M., Tripathi, M., 2016. A new route of magnetic biochar based polyaniline composites for supercapacitor electrode materials. J. Anal. Appl. Pyrolysis 121, 240–257. https://doi.org/10.1016/j.jaap.2016.08.004.

Togibasa, O., Mumfaijah, M., Allo, Y.K., Dahlan, K., 2021. The effect of chemical activating agent on the properties of activated carbon from sago waste. Appl. Sci. 11 (11640), 40. https://doi.org/10.3390/app112411640.

Treeweranuwat, P., Boonyoung, P., Chareonpanich, M., Nueangnoraj, K., 2020. Role of nitrogen on the porosity, surface, and electrochemical characteristics of activated carbon. ACS Omega. 5, 1911–1918. https://doi.org/10.1021/acsomega.9b03586.

Wan, L., Wei, W., Xie, M., Zhang, Y., Li, X., Xiao, R., Chen, J., Du, C., 2019. Nitrogen, sulfur co-doped hierarchically porous carbon from rape pollen as high-performance supercapacitor electrode. Electrochim. Acta 311, 72–82. https://doi.org/10.1016/j.electacta.2019.04.106.

Wang, C., Wu, D., Wang, H., Gao, Z., Xu, F., Jiang, K., 2018. Biomass derived nitrogen-doped hierarchical porous carbon sheets for supercapacitors with high performance. J. Colloid Interface Sci. 523, 133–143. https://doi.org/10.1016/j.jcis.2018.03.009.

Wang, G., Zhang, J., Kuang, S., Zhou, J., Xing, W., Zhuo, S., 2015. Nitrogen-doped hierarchical porous carbon as an efficient electrode material for supercapacitors. Electrochim. Acta 153, 273–279. https://doi.org/10.1016/j.electacta.2014.12.006.

Wang, H., Li, Z., Kwon, J., Holt, C.M.B., Tan, X., Xu, Z., Shalchi, B., Harfield, D., Anyia, A., Stephenson, T., Mitlin, D., 2013. Supercapacitors based on carbons with tuned porosity derived from paper pulp mill sludge biowaste. Carbon 57, 317–328. https://doi.org/10.1016/j.carbon.2013.01.079.

Wulandari, N.N., Rustamaji, H., Fibarzy, W.U., Prakoso, T., Rizkiana, J., Devianto, H., Widiatmoko, P., Nurdin, I., 2021. Production of activated carbon from palm empty fruit bunch as supercapacitor electrode material. IOP Conf. Ser.: Mater. Sci. Eng. 1143, 012004 https://doi.org/10.1088/1757-899x/1143/1/012004.

Xie, M., Duan, S., Shen, Y., Fang, K., Wang, Y., Lin, M., Guo, X., 2016. In-situ-grown Mg(OH)2-derived hybrid α-Ni(OH)2 for highly stable supercapacitor. ACS Energy Lett. 1, 814–819. https://doi.org/10.1021/acsenergylett.6b00258.

Xing, Z., Wang, B., Gao, W., Pan, C., Halsted, J.K., Chong, E.S., Lu, J., Wang, X., Luo, W., Chang, C.H., Wen, Y., Ma, S., Amine, K., Ji, X., 2016. Reducing CO2 to dense nanoporous graphene by Mg/Zn for high power electrochemical capacitors. Nano Energy 11, 600–610. https://doi.org/10.1021/acsenergylett.6b00258.

Yang, W., Li, Y., Feng, Y., 2018. High electrochemical performance from oxygen functional groups containing porous activated carbon electrode of supercapacitors. Materials 11, 2455. https://doi.org/10.3390/ma11122455.

Yu, J., Li, X., Cui, Z., Chen, D., Pang, X., Zhang, Q., Shao, F., Dong, H., Yu, L., Dong, L., 2021. Tailoring in-situ N, O, P, S-doped soybean-derived porous carbon with ultrahigh capacitance in both acidic and alkaline media. Renew. Energy 163, 375–385. https://doi.org/10.1016/j.renene.2020.08.066.

Zhang, J., He, J., Zheng, H., Li, R., Gou, X., 2020. N, S dual-doped carbon nanosheet networks with hierarchical porosity derived from biomass of Allium cepa as efficient catalysts for oxygen reduction and Zn–air batteries. J. Mater. Sci. 55, 7464–7476. https://doi.org/10.1007/s10853-020-04535-4.

Zhang, J., Zhou, J., Wang, D., Hou, L., Gao, F., 2016. Nitrogen and sulfur co-doped porous carbon microsphere: a high-performance electrode in supercapacitor. Electrochim. Acta 191, 933–939. https://doi.org/10.1016/j.electacta.2016.01.150.

Zhang, Y., Zhang, Y., Huang, J., Du, D., Xing, W., Yan, Z., 2016. Enhanced capacitive performance of n-doped activated carbon from petroleum coke by combining ammoxidation with KOH activation. Nanoscale Res. Lett. 11, 0–6. https://doi.org/10.1186/s11671-016-1460-3.

Zhao, G., Chen, C., Yu, D., Sun, L., Yang, C., Zhang, H., Sun, Y., Besenbacher, F., Yu, M., 2018. One-step production of O-N-S co-doped three-dimensional hierarchical porous carbons for high-performance supercapacitors. Nano Energy 47, 547–555. https://doi.org/10.1016/j.nanoen.2018.03.016.

Zhou, J., Shen, H., Li, Z., Zhang, S., Zhao, Y., Bi, X., Wang, Y., Cui, H., Zhuo, S., 2016. Porous carbon materials with dual N, S-doping and uniform ultra-microporosity for high-performance supercapacitors. Electrochim. Acta 209, 557–564. https://doi.org/10.1016/j.electacta.2016.05.127.

Zhou, J., Zhang, Z., Xing, W., Yu, J., Han, G., Si, W., Zhuo, S., 2015. Nitrogen-doped hierarchical porous carbon materials prepared from meta-aminophenol formaldehyde resin for supercapacitor with high rate performance. Electrochim. Acta 153, 68–75. https://doi.org/10.1016/j.electacta.2014.11.075.

Zhu, Y., Chen, M., Zhao, W., 2018. A biomass-derived nitrogen-doped porous carbon for high-energy supercapacitor. Carbon 140, 404–412. https://doi.org/10.1016/j.carbon.2018.09.009.